Adaptive Coherency Matrix Estimation for Polarimetric SAR Imagery Based on Local Heterogeneity Coefficients

Shuai Yang, *Student Member, IEEE*, Qihao Chen, *Member, IEEE*, Xiaohui Yuan, *Senior Member, IEEE*, and Xiuguo Liu, *Member, IEEE*

***Abstract*—Polarimetric synthetic aperture radar (SAR) images usually contain a mixture of homogeneous and heterogeneous regions, which makes estimation of the coherency matrix a very challenging task. In this paper, we propose an adaptive coherency matrix estimation method that employs local heterogeneity coefficient and leverages the sample covariance matrix estimation to the homogeneous components and the fixed-point estimation to the heterogeneous components. Evaluations were conducted with synthetic polarimetric data and real-world SAR imagery, including UAVSAR, RADARSAT-2, and ESAR. Our experimental results demonstrated that the heterogeneity coefficient effectively characterizes the scattering property of ground objects, which enables adaptive estimation of the coherency matrix in high-resolution polarimetric SAR imagery. Our method was able to handle single- and multilook polarimetric SAR imagery gracefully. Compared with the sample covariance matrix estimator, the fixed-point estimator, and the Lee sigma filtering, our method achieved the best performance for retaining the spatial structure, suppressing speckles, and preserving polarimetric information of SAR imagery with different degrees of heterogeneity.**

***Index Terms*—Coherency matrix, heterogeneity coefficient, high resolution, matrix estimation, polarimetric synthetic aperture radar (SAR).**

I. Introduction

SYNTHETIC aperture radar (SAR) systems have been widely used for global Earth observation because of their all-day/all-weather capability and penetration capability. With the sensors being able to emit or receive polarized orthogonal radar waves, polarimetric SAR information allows the discrimination of different scattering mechanisms, generally using polarimetric target decompositions. However, inherent speckle [1] degrades the performance of polarimetric decomposition and target detection [2] and hinders image interpretation and analysis [3].

Manuscript received August 6, 2015; revised December 8, 2015 and May 18, 2016; accepted July 5, 2016. Date of publication July 28, 2016; date of current version September 27, 2016. This work was supported in part by the National Natural Science Foundation of China under Grant 41471355 and Grant 41301477.

S. Yang, Q. Chen, and X. Liu are with the Faculty of Information Engineering, China University of Geosciences, Wuhan 430074, China (e-mail: liuxg318@hotmail.com).

X. Yuan is with the Faculty of Information Engineering, China University of Geosciences, Wuhan 430074, China, and also with the Department of Computer Science and Engineering, University of North Texas, Denton, TX 76203 USA.

Color versions of one or more of the figures in this paper are available online at http://ieeexplore.ieee.org.

Digital Object Identifier 10.1109/TGRS.2016.2589279

To reduce speckles, image filtering has been employed. Lee *et al.* [4] developed a polarimetric SAR filter that uses edge-aligned nonsquare windows and a local statistic filter. A later work of Lee *et al.* [5] proposed an extended Lee sigma filtering method by computing the sigma range based on the theoretical speckle distributions and utilizing a target signature preservation technique. To take into account the physical scattering process, T_{11}, T_{22}, and T_{33} are used to select pixels within the sigma ranges. Pixels within all three ranges are included in the application of the minimum mean square error filter to retain fine details. Ding *et al.* [6] developed a speckle reduction method based on structural decision and a hybrid polarimetric decomposition. Pixels are separated into three categories: bright, dark, and common targets. To protect the polarimetric property, dark and common targets are further separated into four scattering classes, and a dark or a common pixel centered in a sliding window is filtered. Pixels in the same and the neighboring scattering clusters from the same structural category are used to filter. The method differentiates ground objects, and the polarimetric properties are preserved.

In addition to filtering-based methods, coherency (or covariance) matrix estimation has been studied, which is rooted in the characterization of the scattering properties of objects [7]. In medium- or low-resolution polarimetric SAR data, targets of interest require a multivariate statistical description due to the combination of coherent speckle and random vector scattering effects [8]. The scattering vectors from a homogeneous region can be modeled with Gaussian distribution, and the corresponding coherency matrices follow a complex Wishart distribution [9]. In this case, before SAR image analysis, e.g., incoherent decompositions, the underlying coherency matrix of the targets needs to be estimated by the sample covariance matrix (SCM) estimator, which is equivalent to the maximum-likelihood (ML) estimator [3], [10]. Improvements to the SCM method have been proposed. Chen *et al.* [11] developed a double similarity test that uses metrics derived from polarimetric and interferometric information. The test allows a relative large searching window to recruit a sufficient number of homogeneous pixels for coherency matrix estimation, which is also applicable to other unbiased estimators.

The high-spatial-resolution polarimetric SAR images, due to the significantly reduced number of scatterers within a resolution cell, are greatly affected by the heterogeneity [12]. The heterogeneity is usually modeled with the product of a texture

random variable and a Gaussian speckle random vector [13], namely, a spherically invariant random vector (SIRV) model [14]. Based on the SIRV model, Gini and Greco [10] proposed an approximate ML estimator for the normalized underlying matrix using the recursive algorithm, which is known as a fixed-point (FP) estimator [3], under the unknown deterministic texture. Pascal *et al.* [15] demonstrated the uniqueness and convergence of this recursive algorithm for admissible initial conditions. Vasile *et al.* [3] further derived the conventional underlying matrix estimator by estimating the power and normalized underlying matrix and verified that the FP estimator achieves greater accuracy than the SCM estimator in heterogeneous imagery.

In practice, high-resolution polarimetric SAR images usually contain a mixture of homogeneous and heterogeneous regions. The complexity makes estimation of the underlying coherency matrix a very challenging task using the aforementioned methods. To improve the estimation of the coherency matrix, an adaptive method is needed that accounts for different degrees of heterogeneity.

In this paper, we propose a method that estimates the coherency matrix adaptively according to the heterogeneity coefficient. This heterogeneity is measured using a polarimetric whitening filter (PWF) [16] based on the local coefficient of variation, which describes the degree of heterogeneity of local areas. Our method employs local heterogeneity coefficient and leverages the advantages of SCM estimation to the homogeneous components and of fixed-point estimation to the heterogeneous components. The optimal coherency matrix is a weighted summation of the estimations to the mixture of scattering components. Our method is also extended to handle both single- and multilook polarimetric SAR data.

The remainder of this paper is organized as follows. Section II introduces the heterogeneity coefficient and presents our adaptive coherency matrix estimation (ACoME) method for single- and multilook polarimetric SAR imagery. Section III describes our synthetic data and real-world polarimetric SAR imagery and discusses the experimental results. Section IV concludes this paper with a summary.

II. Adaptive Coherency Matrix Estimation

Polarimetric SAR data are available in two forms: the single-look scattering vector and the multilook polarimetric coherency matrix.

Each resolution unit of a fully polarimetric SAR is described by a 2×2 complex scattering matrix $\boldsymbol{S}$, i.e.,

$$\boldsymbol{S} = \begin{bmatrix} S_{\mathrm{HH}} & S_{\mathrm{HV}} \\ S_{\mathrm{VH}} & S_{\mathrm{VV}} \end{bmatrix} \tag{1}$$

where each element represents a complex scattering coefficient; and H and V denote the horizontal and vertical polarization directions, respectively. When reciprocity holds, the cross polarizations are equal, i.e.,

$$S_{\mathrm{HV}} = S_{\mathrm{VH}}. \tag{2}$$

In such a case, the scattering matrix becomes symmetric and can be reduced to a 3-D single-look scattering vector based on the complex Pauli spin matrix basis set, i.e.,

$$\boldsymbol{k} = \frac{1}{\sqrt{2}}[S_{\mathrm{HH}} + S_{\mathrm{VV}} \; S_{\mathrm{HH}} - S_{\mathrm{VV}} \; 2S_{\mathrm{HV}}]^T \tag{3}$$

where $[\cdot]^T$ denotes the transpose of a matrix.

For speckle reduction, an L-look coherency matrix, which is denoted by T, is computed using the average of the scattering vectors of the neighboring pixels as follows:

$$T = \frac{1}{L}\sum_{i=1}^{L} \boldsymbol{k}_i \boldsymbol{k}_i^H \tag{4}$$

where $\boldsymbol{k}_i$ is the scattering vector, $\boldsymbol{k}_i^H$ is the conjugate transpose of $\boldsymbol{k}_i$, and L is the number of looks.

In the rest of this section, we briefly review the SCM and FP estimators. We then introduce the heterogeneity coefficient, followed by our proposed adaptive coherency matrix estimator.

A. SCM Estimator

For a *single-look* polarimetric SAR image, the elements of a vector are generally modeled with a multivariate zero-mean complex Gaussian random process. The probability density function (pdf) is given by the following expression:

$$p_d(\boldsymbol{k}|\Sigma) = \frac{1}{\pi^d|\Sigma|} e^{-\boldsymbol{k}^H \Sigma^{-1} \boldsymbol{k}} \tag{5}$$

where $\Sigma = E[\boldsymbol{k}\boldsymbol{k}^H]$ is the expectation of the underlying coherency matrix, $|\cdot|$ denotes the matrix determinant, and d is the dimension of the target vector ($d = 3$ for monostatic polarimetric SAR acquisitions).

According to (5), a Gaussian stochastic process is characterized by the coherency matrix. Following this model, SCM is the ML estimator of the polarimetric coherency matrix, which is the sample covariance matrix obtained by replacing the mean with the spatial averaging, i.e.,

$$\Sigma_{\mathrm{SCM}} = \langle \boldsymbol{k}\boldsymbol{k}^H \rangle_N \tag{6}$$

where $\langle\cdot\rangle$ denotes sample averaging, and N is the number of samples.

For a *multilook* polarimetric SAR image, if the scattering vectors in (6) are independent, then T follows complex Wishart distribution [9], and its pdf is

$$p(T|\Sigma) = \frac{L^{Ld}|T|^{L-d}}{R(L,d)|\Sigma|^L} e^{-L\mathrm{Tr}(\Sigma^{-1}T)} \tag{7}$$

where $\mathrm{Tr}(\cdot)$ denotes the trace of a matrix, and

$$R(L,d) = \pi^{d(d-1)/2}\Gamma(L)\Gamma(L-1)\cdots\Gamma(L-d+1) \tag{8}$$

where $\Gamma(\cdot)$ is the gamma function. Hence, the SCM estimator is the ML estimator of the coherency matrix, as follows:

$$\Sigma_{\mathrm{SCM}} = \langle T \rangle_N. \tag{9}$$

B. FP Estimator

The Gaussian and Wishart models serve well for homogeneous regions, whereas for heterogeneous regions, the SIRV model is usually used. The coherency matrix T is modeled as the product of a random variable τ and an independent random matrix X, i.e.,

$$T = \tau X \tag{10}$$

where X is the fully developed speckle component and is modeled by Wishart distribution with the covariance matrix parameter $M = E[X]$. τ characterizes the spatial variations in the radar backscattering. This model assumes that all polarizations (in linear or Pauli basis) share the same texture characteristics.

To create such a model, M is normalized such that the trace of M is a constant, i.e., $\mathrm{Tr}(M) = d$. The normalized matrix M reveals polarimetric diversity. The total power is a function of τ, as follows:

$$P = \mathrm{Tr}\left(E[T]\right) = \mathrm{Tr}\left(\tau E[X]\right) = \tau \mathrm{Tr}(M) = \tau d. \tag{11}$$

The pdf of T can be determined by the following integration:

$$p(T) = \int_0^{+\infty} \frac{L^{Ld}}{\tau^{Ld}\Gamma_d(L)} \frac{|T|^{L-d}}{|M|^L} e^{-\frac{L}{\tau}\mathrm{Tr}(M^{-1}T)} p(\tau) d\tau \tag{12}$$

where $p(\tau)$ is the texture pdf associated to the SIRV model, and M can be estimated with the ML method. Gini and Greco [10] derived the approximate ML estimation of M for single-look polarimetric SAR data under the unknown deterministic variable τ.

Given N samples $T_i, i \in \{1, 2, \ldots, N\}$, the ML estimation for pixel i, which is denoted by τ_i, is given by

$$\tau_i = \frac{\mathrm{Tr}(M^{-1}T_i)}{d}. \tag{13}$$

The normalized coherency matrix of deterministic texture is recursively computed as follows:

$$\hat{M}_{\mathrm{FP}}(t+1) = \frac{d}{N} \sum_{i=1}^{N} \frac{T_i}{\mathrm{Tr}\left(\hat{M}_{\mathrm{FP}}(t)^{-1} T_i\right)}. \tag{14}$$

The recursion is initialized with an identifying matrix, and the error is defined by

$$\epsilon_{\mathrm{FP}}(t) = \frac{\left\| \hat{M}_{\mathrm{FP}}(t+1) - \hat{M}_{\mathrm{FP}}(t) \right\|_F}{\left\| \hat{M}_{\mathrm{FP}}(t) \right\|_F} \tag{15}$$

where $\|\cdot\|_F$ denotes the Frobenius norm, and t denotes the number of recursion.

The normalized coherency matrix estimation is independent of the total power. According to (11), (13), and (14), the ML estimation of the power under the unknown deterministic τ is computed as follows:

$$\hat{P} = \mathrm{Tr}\left(M_{\mathrm{FP}}^{-1} T\right). \tag{16}$$

Following (10), we have the coherency matrix of the FP estimator for multilook polarimetric SAR data, i.e.,

$$\Sigma_{\mathrm{FP}} = \frac{\hat{P}}{d} M_{\mathrm{FP}}. \tag{17}$$

When $L = 1$, the FP estimator reduces to the solution for single-look polarimetric SAR data [3].

C. Heterogeneity Coefficient

The coefficient of variation (CV) has been used as an index of homogeneity of SAR images [13]. Lopes *et al.* [17] introduced a CV-based method to filter SAR speckle adaptively. The CV C_I is defined as the ratio of the standard deviation σ_I to the mean $\bar{I}$ of a local region, which is defined by a window of size g in a SAR image, i.e.,

$$C_I = \frac{\sigma_I}{\bar{I}}. \tag{18}$$

The intensity I follows Gamma distribution in a homogeneous area [18], and CV is equal to $\sqrt{1/L}$. On the other hand, in heterogeneous regions, CV is greater than $\sqrt{1/L}$.

Based on the PWF [16] and the multilook PWF [19], the scattering vector $\boldsymbol{k}$ (or coherency matrix T) can be mapped to w as follows:

$$w = \boldsymbol{k}^H \Sigma^{-1} \boldsymbol{k} \text{ or } w = \mathrm{Tr}(\Sigma^{-1} T). \tag{19}$$

w is scale invariant due to the normalized Σ, which is estimated using the SCM estimator described in (6) or (9). The vth moments of w are computed as follows [20]:

$$E[w^v] = \frac{E[\tau^v]}{E[\tau]^v} \frac{1}{L^v} \frac{\Gamma(Ld + v)}{\Gamma(Ld)} \tag{20}$$

where $v \in \Re^+$. The expectation of w is scale invariant and is equal to the dimension, i.e., $E(w) = d$. In a homogeneous region, τ is a constant; the CV of w is $\sqrt{1/Ld}$. The CV of w increases as heterogeneity increases. Hence, we use the CV of w to describe the heterogeneity of the region, i.e.,

$$C_w = \frac{\sigma_w}{d} \tag{21}$$

where σ_w denotes the standard deviation of w. Since d is a constant, the degree of heterogeneity of the local area in a polarimetric SAR image is proportional to σ_w, i.e.,

$$C = dC_w = \sigma_w. \tag{22}$$

To handle different degrees of heterogeneity, thresholds C^- and C^+ are used to process the estimation adaptively, as follows.

1) For homogeneous regions that have the heterogeneous coefficient less than C^-, i.e., $C \leq C^-$, the coherency matrix is close to the SCM estimation.
2) For highly heterogeneous regions that have the heterogeneous coefficient greater than C^+, i.e., $C \geq C^+$, the coherency matrix is close to the fixed-point estimation.

3) For regions with a mixture of homogeneous and heterogeneous components that have the heterogeneous coefficient in between C^- and C^+, i.e., $C^- < C < C^+$, the coherency matrix is a combination of SCM estimation and fixed-point estimation.

According to (20) and (22), in a homogeneous area, the threshold $C^- = \sqrt{d/L}$. Determining the threshold C^+ is more challenging. It varies according to the images under processing and is also influenced by the objective of the expected outcome. A lower C^+ allows less distortion to the details, whereas a higher C^+ is usually applied if speckle suppression is pursued. In the previous research, thresholds have been proposed. For instance, $C^T = \sqrt{1 + (2/L)}$ proposed by Touzi *et al.* [21] is a threshold for edge detection, which is independent from the dimension. In the polarimetric case, $C^T = \sqrt{d^2 + (2d/L)}$ based on (19), weighs the dimension much greatly. That is, C^T is proportional to d and inversely proportional to $\sqrt{L}$. We propose a threshold that imposes equal proportion to d and L, and hence, the two thresholds are computed as follows:

$$\begin{cases} C^- = \sqrt{\frac{d}{L}} \\ C^+ = \sqrt{\frac{\lambda d}{L}} \end{cases} \tag{23}$$

where $\lambda \geq 1$ is a margin parameter that decides the range of the mixture of homogeneous and heterogeneous components. It is a constant and is specified empirically. Detailed discussion is presented in Section III-F.

The calculation of (23) needs to estimate the equivalent number of looks (ENL), which describes the degree of averaging of polarimetric SAR images. For single-look polarimetric SAR data, $L = 1$; for multilook polarimetric SAR data, the ENL is estimated using matrix log-cumulants [22] by

$$\sum_{v=0}^{d-1} \psi^{(v)}(\hat{L} - v) - d \ln \hat{L} = \langle \ln |T| \rangle - \ln |\Sigma| \tag{24}$$

where $\psi^{(v)}(\cdot)$ is the vth-order multivariate polygamma function. In the estimation process, the estimation value $\hat{L}$ of the constant L can be obtained by selecting samples in homogeneous areas without texture from polarimetric SAR image. To estimate the ENL, samples are selected from the image according to the local heterogeneity coefficient. Regions with the lowest local heterogeneity coefficient are identified, and the size of the candidate region must be greater than 900 pixels. In our method, more than one region is selected to make estimation, and the average is used as the final estimation of ENL. Among many ground objects, calm lakes and artery roads are the primary choices for the computation.

D. ACoME Method

Our ACoME method is based on local heterogeneity coefficient and leverages the advantages of SCM estimation to the homogeneous components and of fixed-point estimation to the heterogeneous components. The optimal coherency matrix estimation is a weighted summation of the estimations to the mixture of scattering components.

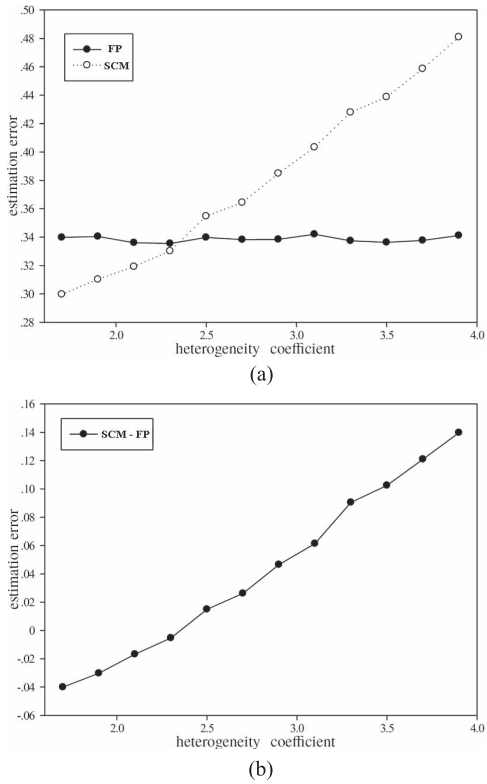

Fig. 1. Estimation error of synthetic polarimetric data. (a) SCM and FP. (b) SCM minus FP.

The weights depend on the heterogeneity coefficient C. To determine the weights, the estimation error ϵ of the coherency matrix is computed as follows [3]:

$$\epsilon = \frac{1}{N} \sum_{i=1}^{N} \frac{\|\hat{M}_i - M^*\|_F}{\|M^*\|_F} \tag{25}$$

where M^* represents the reference normalized coherency matrix for data simulating, and N is the number of samples.

Fig. 1(a) illustrates the change of the estimation error ϵ with respect to the heterogeneity coefficient C. The error of the SCM estimator increases with the increase of C, whereas the error of the FP estimator remains mostly unchanged. The difference of the errors is shown in Fig. 1(b), which is mostly linear. When C is small, the SCM estimator outperforms the FP estimator, and at a certain point, the error from SCM surpasses that from FP.

Intuitively, the intersection of the estimation error by the SCM and FP methods, as shown in Fig. 1(a), indicates a possible way of combining the coherency matrix estimations. However, in practice, such intersection is unnecessarily a clear cut. Multiple divisions of the heterogeneity coefficient are needed to characterize the transition region. Hence, the optimal coherency matrix can be achieved with the summation of the homogeneous and heterogeneous components as follows:

$$T = \sum_i \beta_i T_i \tag{26}$$

where T_i is the estimation of the coherency matrix given a heterogeneity coefficient, and β_i is the weight. In this paper, we divide the entire range of the heterogeneity coefficient into three

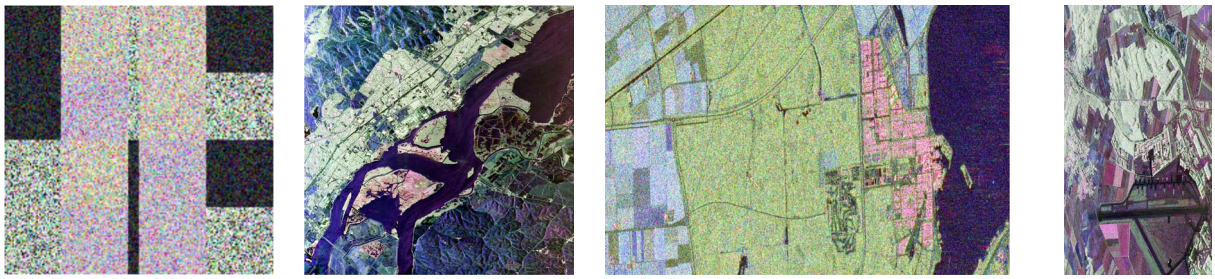

(a) (b) (c) (d)

Fig. 2. Examples of our experimental images. (a) Synthetic image. (b) L-band UAVSAR. (c) C-band RADARSAT-2. (d) L-band ESAR.

regions with the two thresholds given in (23), and the weights are computed as follows:

$$\beta = \begin{cases} 0, & C \le C^- \\ \frac{C-C^-}{\Delta C}, & C^- < C < C^+ \\ 1, & C \ge C^+ \end{cases} \tag{27}$$

where ΔC is the range of the transition region of the heterogeneity coefficient from homogeneous SAR to heterogeneous SAR. Hence, our proposed adaptive estimator consists of a linear combination of two components, as follows:

$$T = (1-\beta)\dot{T} + \beta\ddot{T} \tag{28}$$

where $\dot{T}$ denotes the estimation from the homogeneous components, and $\ddot{T}$ denotes the estimation from the heterogeneous components. In our implementation, the SCM method was used to estimate $\dot{T}$, and the FP method was used to estimate $\ddot{T}$. It is proven that the SCM and FP estimators are unbiased [23]. According to (28), it is easy to prove that the linear combination of the SCM and FP estimators is also unbiased. Algorithm 1 summarizes our ACoME method.

Algorithm 1 ACoME algorithm.

1: INPUT: polarimetric SAR image I and window size g.
2: OUTPUT: coherency matrix T.
3:
4: **for** $I(x,y) \in I$ **do**
5: Compute $C(x,y)$ following (19) and (22) with the given g.
6: **end for**
7: Compute C^- and C^+ following (23).
8: **for** $I(x,y) \in I$ **do**
9: Compute weight $\beta(x,y)$ given $C(x,y)$ following (27).
10: Compute coherency matrix for homogeneous component $\dot{T}$ following (6) (single look) or (9) (multilook).
11: Compute $\hat{M}_{\mathrm{FP}}$ and $\hat{P}$ following (14) and (16).
12: Compute coherency matrix for heterogeneous component $\ddot{T}$ following (17).
13: **end for**
14: The coherency matrix is the linear combination of $\dot{T}$ and $\ddot{T}$ as follows:

$$T = (1-\beta)\dot{T} + \beta\ddot{T}.$$

III. Experimental Results

A. Experimental Data and Settings

To quantitatively evaluate our proposed method, synthetic polarimetric SAR data were created. To our best knowledge, Wishart distribution [9] has been used for generating homogeneous SAR imagery, whereas K-distribution [24] is used to simulate heterogeneous regions in SAR imagery. In K-distribution, the shape factor α determines the degree of heterogeneity of the synthetic data [20], i.e.,

$$\alpha = \frac{Ld^2 + d}{L\sigma_w^2 - d}. \tag{29}$$

There is a correspondence between α and C, since σ_w^2 is equal to the square of C, which means that one can obtain synthetic data of specific C by modifying α. In our synthetic SAR data, as shown in Fig. 2(a), we varied α to create regions of different heterogeneities. Each synthetic image consists of multiple regions that are of different geometric shapes and degrees of heterogeneity. The schematic is shown in Fig. 7(b). To simulate ground objects such as roads and rivers, narrow regions were created in the synthetic imagery.

In addition to the synthetic data sets, we used real-world SAR imagery from three different sources as follows: 1) L-band UAVSAR data of Hayward in the U.S. by the Alaska Satellite Facility acquired on February 12, 2014; the size of the image is 2500 × 2500 pixels, with a spatial resolution of approximately 4.997 m × 7.2 m (range × azimuth), as shown in Fig. 2(b); 2) C-band RADARSAT-2 fine quad-polarization data of Flevoland, Holland, acquired on April 2, 2008; the size of the image is 800 × 1200 pixels, with a spatial resolution of 12 m × 8 m (range × azimuth), as shown in Fig. 2(c); 3) L-band ESAR images of Oberpfaffenhofen, Germany, which are single look, with a spatial resolution of 1.5 m × 0.89 m (range × azimuth); the size of the image is 1540 × 2816 pixels, as shown in Fig. 2(d).

To analyze polarimetric information from coherency matrix, target decomposition was employed in our evaluation. There are a number of strategies to evaluate the effects of various types of ground reflectors [25]–[29]. A review of model-based target decomposition is available in [30]. In our study, we adopted the Yamaguchi four-component decomposition [25], [26] due to its wide applicability and effectiveness in analyzing homogeneous and heterogeneous regions.

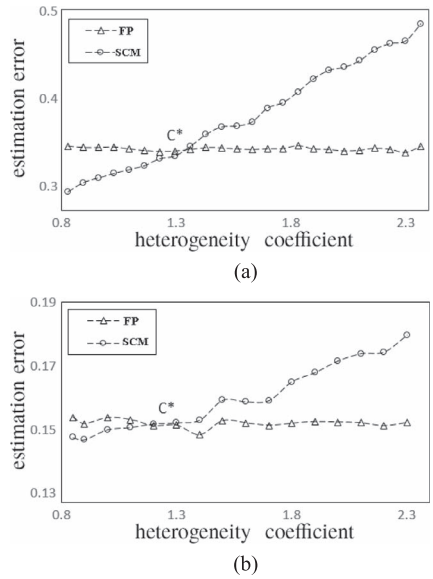

Fig. 3. Estimation error of the synthetic data. (a) Single-look case consists of 24 sampling points. (b) Multilook case ($L = 4$) consists of 16 sampling points. The data are simulated by K-distribution, which covers the real situation of different heterogeneities.

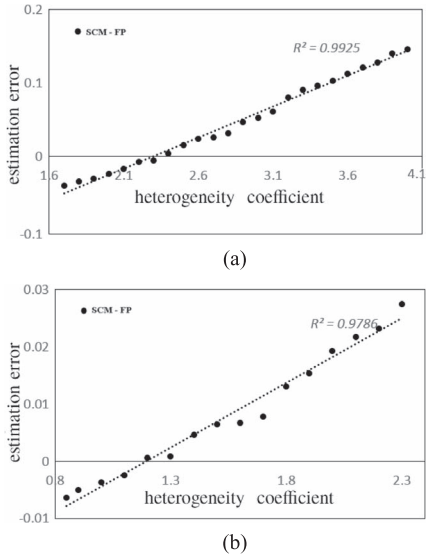

Fig. 4. Estimation error difference figures of synthetic data. (a) Single-look case consists of 24 sampling points. (b) Multilook case ($L = 4$) consists of 16 sampling points.

A parameter used in our method is λ in (23), which decides the upper bounds of the mixture of homogeneous and heterogeneous regions. In our experiments, we set λ to 3 based on our empirical evaluation. Detailed experiments and discussion are presented in Section III-F.

B. Error Linearity and Estimation of the Thresholds

Fig. 3 illustrates the estimation error of SCM and FP using our synthetic data. It is clear that the error of the SCM estimator increases as the heterogeneous coefficient C increases in both the single- and multilook cases. The error of the FP estimator, on the other hand, changed slightly with respect to C. The difference between ϵ_{SCM} and ϵ_{FP} is shown in Fig. 4.

We adopt the coefficient of determination R^2 to evaluate the "goodness of fit" of the linear model to the estimation error, which is computed as follows:

$$R^2 = \frac{\sum_i (\hat{f}_i - \bar{f})^2}{\sum_i (\hat{f}_i - f_i)^2} \tag{30}$$

where $\bar{f}$ is the mean of the observed data, and $\hat{f}_i$ denotes the model prediction. The coefficient of determination R^2 is a statistical measure of how well the model approximates the real data. An R^2 of 1 indicates that the model perfectly fits the data. In our experiments, the coefficients of determination are 0.9925 and 0.9786 for the two cases shown in Fig. 4(a) and (b), respectively, which indicates that the linear model fits the estimation error closely for both the single- and multilook cases.

Table I lists the thresholds for the single- and multilook SAR imagery. $\tilde{C}^+$ is the optimal threshold that represents the lower bound of the heterogeneity coefficient for the highly heterogeneous components. It is symmetric to C^- with respect to C^*. That is, $\tilde{C}^+ = 2C^* - C^-$. C^T is the threshold computed with the method in [21]. C^+ is our proposed estimation calculated with (23), where λ is 3. The last two columns are the absolute differences of C^T and C^+ to the reference $\tilde{C}^+$. Compared with C^T, C^+ gives smaller differences for both the single- and multilook cases, which indicates that C^+ provides a better estimation of the threshold for the highly heterogeneous components.

TABLE I
THRESHOLDS OF POLARIMETRIC SAR IMAGERY. $\tilde{C}^+$ IS A REFERENCE THRESHOLD CALCULATED FROM THE SYNTHETIC DATA; C^T IS THE THRESHOLD COMPUTED WITH THE METHOD IN [21]. ΔC^T AND ΔC^+ ARE THE DIFFERENCES OF C^T AND C^+ TO $\tilde{C}^+$

ENL	C^-	C^*	$\tilde{C}^+$	C^T	C^+	ΔC^T	ΔC^+
L=1	1.73	2.35	2.97	3.87	3	0.9	0.03
L=4	0.87	1.2	1.53	3.24	1.5	1.71	0.03

C. Analysis of Window Size for Computing Local Heterogeneity Coefficient

The window size determines the granularity of the calculation of the heterogeneity coefficient, which is a key to characterize the local heterogeneity of SAR imagery. Using synthetic imagery [see example in Fig. 2(a)], we studied the effects of window size. As previously stated, our synthetic images were created following the Wishart and K-distributions.

Fig. 5 illustrates the results of using different window sizes. With a 3×3 window, the speckles were barely suppressed, whereas with a 9×9 window, the speckles were mostly even out. However, a 9×9 window also created artifacts along the boundaries of the heterogeneous regions. In contrast, both window sizes 5×5 and 7×7 exhibited superior results with respect to both speckle reduction and boundary preservation.

The quality of the processed polarimetric SAR image can be indirectly evaluated with an image segmentation method

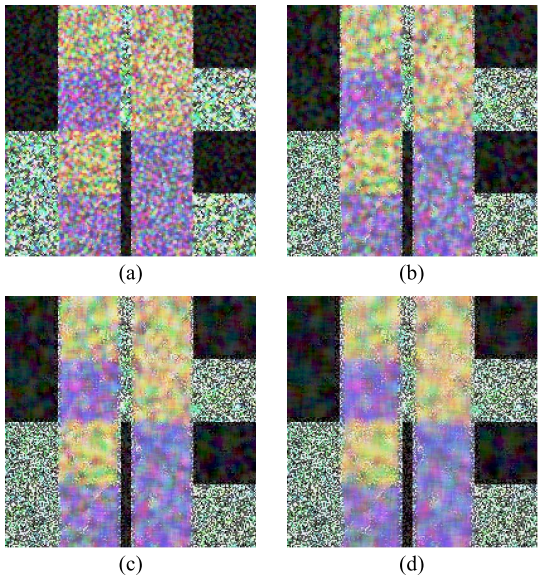

Fig. 5. Estimate results of different window sizes with the proposed estimator. (a) 3 × 3. (b) 5 × 5. (c) 7 × 7. (d) 9 × 9.

with a reference image (the synthetic image in our case). Segmentation of a noisy image usually results in erroneous delineation, whereas an overly smoothed image loses details of the boundaries between ground objects. Both the aforementioned situations may lead to inaccurate boundaries of segmentation results. To quantitatively evaluate the effect of window size, we used the degree of overlap ρ as the metric. Let I denote the reference segmented SAR image that consists of regions representing ground objects, each of which is of a distinct degree of heterogeneity to the neighboring regions. I_l denotes a subregion in I that corresponds to object l. Let J denote the segmentation result from the processed SAR image and J_l denote a subregion in J for object l. Hence, the difference between I and J quantifies the agreement of object structure. The degree of overlap is computed as follows:

$$\rho = \frac{1}{N}\sum_{l=1}^{N}\frac{I_l \cap J_l}{(I_l + J_l - I_l \cap J_l)} \tag{31}$$

and $\rho \in [0, 1]$, where $\rho = 1$ indicates the highest agreement and hence the best performance.

Without loss of generality, our experiments employed the polarimetric SAR segmentation method proposed in [31]. Note that the narrow regions in the middle of the synthetic images were of 8 pixels in width, which simulated ground objects such as roads and rivers. The limited width restrained the window size in our experiment. For the ones that greatly exceed the scale, the computation of heterogeneity is greatly influenced by pixels in the neighboring region with different degrees of heterogeneity. Hence, our window size ranges from 3 to 9.

Table II lists our experimental results. Five repetitions were conducted for each size, and both average and standard deviation (STD) are reported. In four of the five repetitions, the window size of 5 × 5 yielded the highest agreement. The average ρ of 5 × 5 was the highest among all. As the window size increased, ρ decreased considerably. The STDs in all cases were fairly small. The window size 7 × 7 resulted in the second highest agreement on average with the smallest STD. However, compared with the window size 5 × 5, the degree of overlap using the window size 7 × 7 was inferior. One thing worth mentioning is that a small window size may not be sufficient for homogeneous regions, whereas for heterogeneous regions, a large window size may be surplus. Hence, an overall window that achieves a balance to a variety of heterogeneities is preferred. Based on the former consideration and our experiment results, it is clear that a window size of 5 × 5 was an appropriate choice, which was used in the rest of our experiments.

TABLE II
AVERAGE DEGREE OF OVERLAP USING DIFFERENT WINDOW SIZES. THE RESULTS ARE THE AVERAGE OF FIVE SETS OF SYNTHETIC SAR DATA

Repetition	3 × 3	5 × 5	7 × 7	9 × 9
1	0.8742	**0.9482**	0.8989	0.8757
2	0.9069	**0.9389**	0.9120	0.8722
3	0.9235	**0.9347**	0.9179	0.8843
4	0.8150	**0.9537**	0.9123	0.8485
5	**0.9246**	0.9177	0.9114	0.8841
Mean	0.8888	**0.9386**	0.9105	0.8730
STD	0.0460	0.0139	0.0070	0.0147

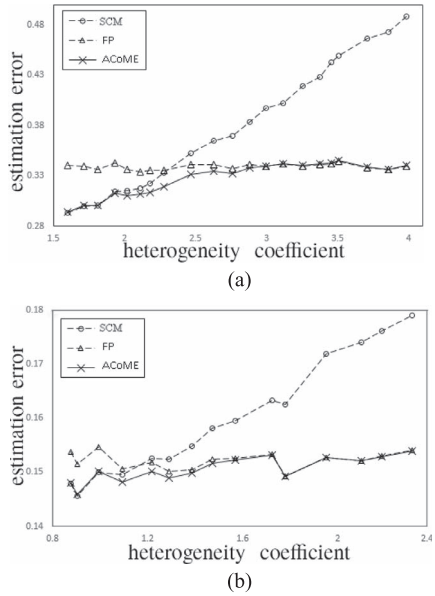

Fig. 6. Estimation error with respect to different heterogeneity coefficients. (a) Single-look case. (b) Multilook case ($L = 4$). The data were simulated with K-distribution, which covers the real situation of different heterogeneities. The experiment is chosen from five similar experiment results.

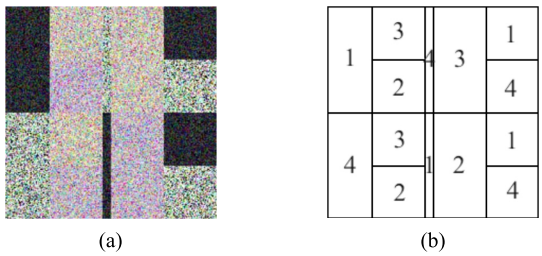

Fig. 7. Synthetic polarimetric SAR image and the schematic of region types. (a) Synthetic SAR image. (b) Diagram of region types.

TABLE III
AVERAGE DECOMPOSITION ERROR OF THE SYNTHETIC SAR IMAGERY

Het.	1				2				3				4			
Type	Odd.	Dbl.	Vol.	Hlx.	Odd.	Dbl	Vol.	Hlx.	Odd.	Dbl	Vol.	Hlx.	Odd.	Dbl	Vol.	Hlx.
R^*	0.429	0.188	0.341	0.042	0.311	0.355	0.299	0.036	0.235	0.419	0.176	0.170	0.271	0.182	0.404	0.143
SCM	0.244	0.350	0.328	0.987	**0.358**	**0.234**	0.300	0.798	0.433	**0.165**	**0.903**	**0.506**	0.564	0.602	0.429	0.511
FP	0.248	0.328	0.342	0.988	0.401	0.262	0.334	0.907	0.473	0.191	0.953	0.512	**0.516**	0.546	0.408	**0.509**
Sigma	0.278	0.363	0.350	0.931	0.405	0.272	0.340	0.813	0.500	0.217	0.976	0.526	0.736	0.805	0.522	0.586
ACoME	**0.213**	**0.289**	**0.306**	**0.904**	**0.358**	**0.234**	**0.297**	**0.795**	**0.431**	**0.165**	0.904	0.507	**0.516**	**0.542**	**0.407**	0.510

D. Performance Assessment

1) Quantitative Analysis Using Synthetic Data: Fig. 6 depicts the average estimation error of the SCM, FP, and ACoME methods with respect to different heterogeneity coefficients using both the single- and multilook polarimetric SAR images [see Fig. 6(a) and (b), respectively]. In this experiment, synthetic images of different degrees of heterogeneity were created, and five repetitions for each C were conducted to report the average error. As shown in Fig. 6(a), ACoME exhibited a very similar performance to that of SCM in the lower end of the heterogeneity coefficient, i.e., $C < 2$. In the upper end of the heterogeneity coefficient, i.e., $C > 3$, the error or ACoME is close to that of FP. In the middle range of the heterogeneity coefficient, ACoME achieved the smallest error compared with SCM and FP. Similar trends were observed in the multilook polarimetric SAR case in Fig. 6(b). It is evident that our proposed method achieved the best performance with different degrees of heterogeneity.

To closely simulate the realistic SAR data, we created synthetic images with a mixture of different degrees of heterogeneity. Fig. 7 illustrates a synthetic single-look polarimetric SAR image that consists of 14 regions of four heterogeneity categories. Category 1 is a homogeneous case created following Wishart distribution. Categories 2, 3, and 4 are heterogeneous cases following K-distribution with various degrees of heterogeneity from low to high, respectively. The reference matrices T^* used for simulation are sampled from real polarimetric SAR data. For instance, urban region was used for high heterogeneity. The images were decomposed into four basic scattering types (odd scatterers, double scatterers, volume scatterers, and helix scatterers) using the Yamaguchi decomposition method, and the corresponding coherency matrix was computed to obtain the reference power of each scattering type P^*.

The error of each scattering mechanism in each type of regions is

$$\epsilon_i = \frac{1}{N_k} \sum_{(x,y)\in k} \frac{|R_i(x,y) - R_i^*|}{R_i^*} \tag{32}$$

where (x, y) denotes a pixel location regions of the same category k, $k \in \{1, 2, 3, 4\}$, and $i \in \{\text{odd}, \text{double}, \text{volume}, \text{helix}\}$. $R_i(x, y) = P_i(x, y)/P(x, y)$ is the normalized power for the scattering type i, and $R_i^* = P_i^*/P^*$ is the corresponding normalized reference power that remains the same for the same scattering mechanism. N_k is the total number of pixels in all regions of category k. Hence, the total error of regions of the same heterogeneity category k is a weighted summation as follows:

$$\mathcal{E}_k = \sum_i R_i^* \epsilon_i. \tag{33}$$

TABLE IV
TOTAL ERROR OF REGIONS OF THE SAME HETEROGENEITY CATEGORY OF THE SYNTHETIC SAR IMAGERY AND THE AVERAGE ERROR $\bar{\mathcal{E}}$

Error	$\mathcal{E}_1$	$\mathcal{E}_2$	$\mathcal{E}_3$	$\mathcal{E}_4$	$\bar{\mathcal{E}}$
SCM	0.324	0.313	**0.416**	0.509	0.391
FP	0.326	0.350	0.446	0.477	0.400
Sigma	0.346	0.353	0.470	0.641	0.453
ACoME	**0.288**	**0.312**	**0.416**	**0.476**	**0.373**

(a) (b) (c)

Fig. 8. Images of the research area. Blue depicts the homogeneous regions, green depicts the moderately heterogeneous regions, and red depicts the highly heterogeneous regions. (a) UAVSAR. (b) Optical. (c) Heterogeneity.

The average error across all four scattering types and heterogeneity categories is

$$\bar{\mathcal{E}} = \frac{1}{4} \sum_k \mathcal{E}_k. \tag{34}$$

Table III lists the decomposition errors of the four different scattering types (odd, double, volume, and helix) in the four heterogeneity categories. R^* gives the reference normalized power, which is also used in computing the total error of regions with the same heterogeneity category in (33). The minimum errors are highlighted in bold. Our proposed ACoME achieved the best performance by having the lowest error in most cases. Among all 16 cases, ACoME resulted in the lowest error in 13 cases. The other three cases are within 0.1% margin. The last column in Table IV gives the overall average error following (34). The improvement was significant. The overall average error reduction with respect to Lee sigma filtering was 17.66%, and the error reductions with respect to the SCM and FP methods were 4.60% and 6.75%, respectively.

Table IV lists the total error of regions of the same heterogeneity category $\mathcal{E}_i$ and the average error $\bar{\mathcal{E}}$. By taking into consideration the weights R^* in Table III, ACoME exhibited the lowest error in all heterogeneity categories and in terms of the average error. It is also interesting to note that SCM achieved a lower error than FP in $\mathcal{E}_1$, $\mathcal{E}_2$, and $\mathcal{E}_3$, whereas FP resulted in better performance in the heterogeneous case $\mathcal{E}_4$.

2) Assessment Using Multilook Polarimetric SAR Imagery: Fig. 8 illustrates an example of the multilook polarimetric SAR image in PauliRGB [see Fig. 8(a)] and the corresponding optical image [see Fig. 8(b)]. The field of view of this image consists of forests, urban areas, a river, and a mixture of

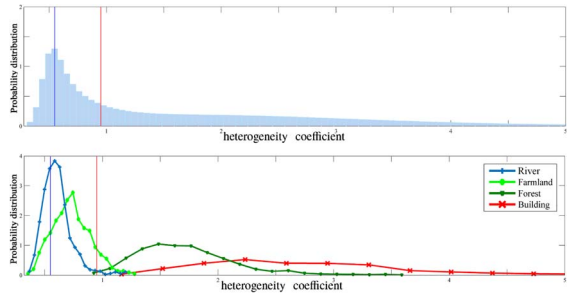

Fig. 9. Heterogeneity coefficient distribution. (Top panel) Distribution of the entire UAVSAR image. (Bottom panel) Distributions of different land objects (river, farmland, forest, and buildings). The vertical lines in each plot mark the thresholds used in our experiments, i.e., C^- (blue) and C^+ (red).

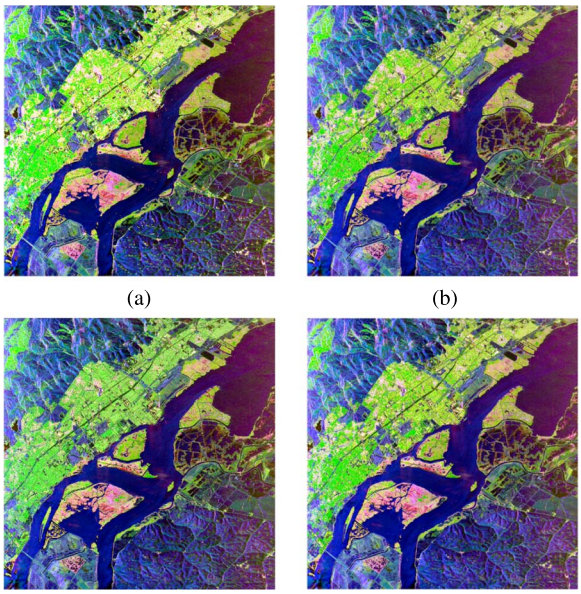

Fig. 10. Results of the postestimated images (red: double component; green: volume component; blue: odd component). (a) SCM. (b) FP. (c) Sigma. (d) ACoME.

farmland and bare soil. The heterogeneity coefficient map of the polarimetric SAR image is shown in Fig. 8(c).

Fig. 9 depicts the distribution of the heterogeneity coefficient C. The top panel shows the distribution of C of the entire image. The vertical lines mark the two thresholds. Given the size of the areas of river and farmland (soil), the majority of the image is close to homogeneous and moderately heterogeneous regions. The two thresholds are fairly close, which are $C^- = 0.55$ and $C^+ = 0.95$. The bottom panel depicts the distribution of heterogeneity coefficient of different ground objects. The heterogeneity coefficients of urban area (in red) and forest (in dark green) dominate the higher end of the distribution, whereas the river (in blue) dominates the lower end of the distribution. The farmland (in light green) and part of the river give different degrees of heterogeneity. The heterogeneity coefficient clearly presents an effective means of characterizing the scattering property of the mixture of land objects.

Fig. 10 illustrates the results of an example SAR image using SCM, FP, Lee sigma filtering, and our proposed ACoME method. Limited by the number of channels of a color image, only three ground scattering object types were colored with red (double scatterer), green (volume scatterer), and blue (odd scatterer). The window size used in computing the heterogeneity coefficient was 5×5, and the window size of the Lee sigma filtering was 7×7. Yamaguchi decomposition was employed to split the image into four types of scattering objects. Due to the scale of the panels, the effects of the different methods are almost invisible, with a few large smoothing effects viewable in the center left (bright green) and lower left corner (light red).

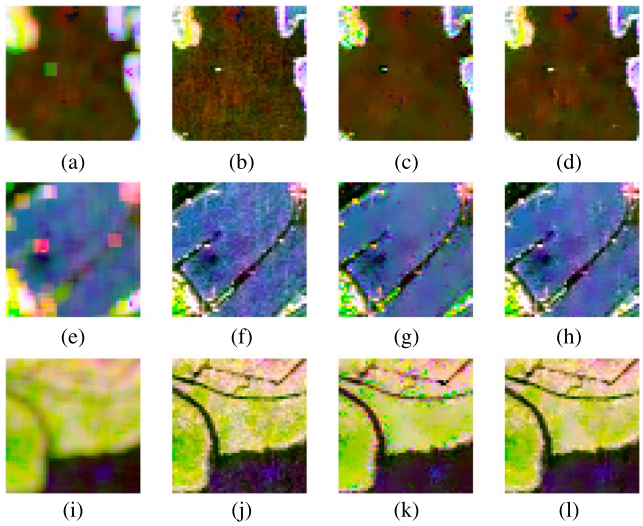

Fig. 11. Zoom-in views of the results using the SCM, FP, Lee sigma filtering, and ACoME methods. The panels depict (a)–(d) water body, (e)–(h) road, and (i)–(l) river bank. (a) SCM. (b) FP. (c) Sigma. (d) ACoME. (e) SCM. (f) FP. (g) Sigma. (h) ACoME. (i) SCM. (j) FP. (k) Sigma. (l) ACoME.

To have a clear understanding of the effects of the aforementioned methods, Fig. 11 illustrates the zoom-in views of three regions with characteristic targets: water body with a boat [see Fig. 11(a)–(d)], road [see Fig. 11(e)–(h)], and river bank [see Fig. 11(i)–(l)]. SCM generated smooth regions in all three cases, which characterized the homogeneous regions well. However, it diffused objects with high scattering contrast. The boat in water [see Fig. 11(a)] and the roads [see Fig. 11(e)] are mostly suppressed. In contrast, FP preserved the fine details of the objects together with the speckle noise, as shown in Fig. 11(b), (f), and (j). The Lee sigma filtering was able to handle homogeneous and heterogeneous objects with success. However, the Lee sigma filtering was unable to fully adapt to the target scattering properties, particularly in the heterogeneous areas. Results of the Lee sigma filtering [see Fig. 11(c), (g), and (k)] depict inconformity in some fine features such as road and river bank. In all these cases, the ACoME method was able to adapt to the spatial dynamics of the ground objects [see Fig. 11(d), (h), and (l)] and produced accurate characterization of the homogeneous and heterogeneous targets. It is evident that the ACoME method exhibited the best performance among all and it retained both the geometric and polarimetric information.

Table V lists the quantitative evaluation of the aforementioned methods based on the average power and the power standard deviation. Fig. 12 illustrates the study site, which was divided into two regions: region A represents the boat, and

TABLE V
STATISTICS OF POWER OF COMBINATION OF REGION A AND REGION B

	SCM	FP	Sigma	ACoME
Mean	0.01790	0.02448	0.01831	0.02438
STD	0.01039	0.09433	0.05472	0.09434

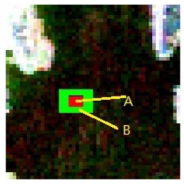

Fig. 12. Study site. The red box highlights the boat (part A), and the green box highlights the surrounding water in close vicinity (part B).

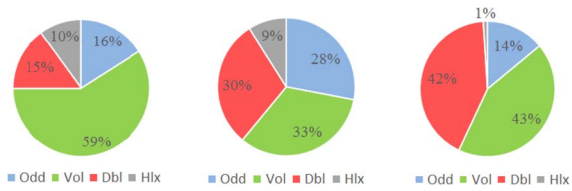

Fig. 13. Power decomposition of the scattering components in region A. (Left to right) Results of SCM, Sigma, and ACoME (equivalent to FP).

region B represents the water in the close vicinity. Due to the smoothing effect, the average power of SCM within these two regions was the lowest compared with that of the other three methods. Although the ACoME method integrated estimations from homogeneous and heterogeneous components, it retained most features, and hence, the overall power remained fairly high. Most importantly, the standard deviation reveals that ACoME exhibited the most discriminant power between the boat and the background water body, which is vital in applications such as target detection.

For region A, we decomposed it into the four basic scattering components (odd, double, volume, and helix). Fig. 13 illustrates the power contribution from different scattering components. Given that the boat is a man-made object with many reflective surfaces, we expect that the contributions from double and helix scatterers are substantial. Note that, for region A, FP and ACoME exhibited highly similar results due to high degree of heterogeneity. The contributions to the total scattering power from double and helix scatterers are 25% and 39% by the SCM method and the Lee sigma filtering, respectively, whereas the contribution from double and helix scatterers estimated based on our ACoME method is 43%, which indicates that the ACoME method is able to characterize the dominant scattering properties and hence serve further applications, such as ship detection, with greater accuracy.

3) Assessment Using Single-Look Polarimetric SAR Imagery: Fig. 14 illustrates an example of the spaceborne single-look C-band RADARSAT-2 imagery of Flevoland, Holland, and the corresponding optical image. It is visible from the optical image that the ground objects include lake, farmland, forest, and urban area, which provides a collection of scattering mechanisms.

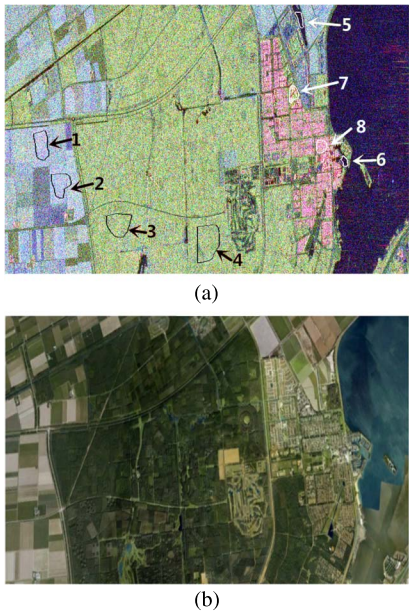

Fig. 14. Example image of RADARSAT-2 data of Flevoland, Holland. (a) RADARSAT-2 SAR image in PauliRGB. (b) Optical image. Sample regions are marked with numbers in (a).

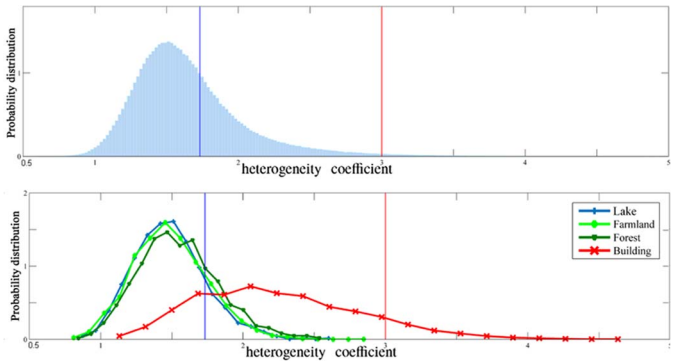

Fig. 15. Heterogeneity coefficient distribution. (Top panel) Distribution of the entire RADARSAT-2 image. (Bottom panel) Distributions of different land objects (calm lake, farmland, forest, and buildings). The vertical lines in each plot mark the thresholds, i.e., C^- (blue) and C^+ (red).

The distribution of the heterogeneity coefficient is shown in Fig. 15. The top panel shows the distribution of C of the entire image. The bottom panel depicts the distribution of the heterogeneity coefficient of different ground objects. The distributions of forest (in dark green), farmland (in light green), and calm lake (in blue) are very similar and dominate the lower end of the distribution. Given that $L = 1$, following (23), the heterogeneity thresholds were $C^- = 1.73$ and $C^+ = 3.00$, which are marked with vertical lines in both panels. Different from the UAVSAR, the forest in RADARSAT-2 appears more homogeneous. The building area (in red) dominates the higher end of the distribution. The heterogeneity coefficient facilitates the characterization of the scattering properties of the mixture of land objects in single-look polarimetric SAR imagery.

By selecting eight regions from the example RADARSAT-2 image [see Fig. 14(a)], Fig. 16 illustrates the normalized power of four basic scattering components in different ground objects. The labels on the x-axis correspond to the regions depicted

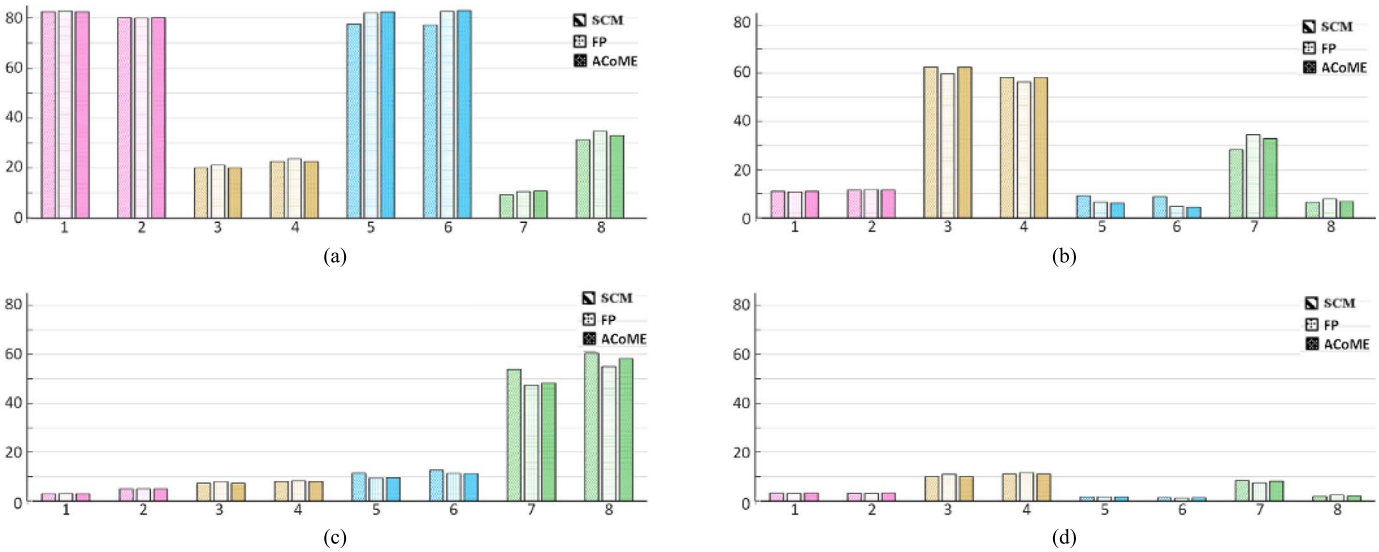

Fig. 16. Normalized power of the decomposition of four different land objects. Each group consists of three bars that represent the results from SCM, FP, and ACoME. The labels on the x-axis correspond to the regions depicted in Fig. 14(a). (a) Odd scatterer. (b) Volume scatterer. (c) Double scatterer. (d) Helix scatterer.

in Fig. 14(a). Each group (depicted in the same color) of bars consists of results of SCM, FP, and ACoME. Regions 1 and 2 are farmlands; regions 3 and 4 are forests; regions 5 and 6 are water body; regions 7 and 8 are buildings. It is clear that the majority of the scattering power for the farmlands and water body was from odd scatterers, whereas the majority of the scattering power for forests was from volume scatterers. The urban area had the most complex scattering power mixture, and double scatterers dominated.

For farmlands and forests, ACoME exhibited similar performance to SCM. This is partly due to the homogeneous scattering property of these two types of land objects. In contrast, FP was inferior in characterizing these objects, as shown in the volume scatterer panel [see Fig. 16(b)]. The shortage from volume scattering power appeared in the contributions from helix and odd components. As to the urban areas, buildings and man-made structures present many double and some helix scatterers. The high degree of heterogeneity made ACoME and FP better means of characterizing land objects, which is demonstrated in Fig. 16(c). Both ACoME and FP exhibited more power contribution than SCM. In addition, the existence of trees in urban areas also made a significant amount of power contribution from the volume scatterers. In water bodies, the scattering power of odd components from ACoME and FP exceeded that from SCM, which reflects the actual scattering property of water body. In summary, our ACoME method facilitated an adaptive means of characterizing various land objects with precision.

E. Validation With High-Resolution Polarimetric SAR Imagery

High-resolution polarimetric SAR images usually contain more details than moderate-resolution ones, which alters the scattering power of the ground objects. To evaluate the performance of the proposed method with high-resolution polarimetric SAR data, we used a single-look L-band ESAR image of Oberpfaffenhofen, Germany, as shown in Fig. 17. The spatial

Fig. 17. ESAR image of Oberpfaffenhofen in PauliRGB. The top left box represents samples of housing area in Fig. 19(a)–(d). The bottom right box represents samples of a double-bounce reflector in Fig. 19(e)–(h). The top right box represents samples of parking lot with rows of cars in Fig. 19(i)–(l).

resolution is 1.5 m $\times$ 0.89 m (range $\times$ azimuth). The distribution of the heterogeneity coefficients is shown in Fig. 18, in which the top panel depicts the coefficient distribution of the high-resolution ESAR image. The bottom panel in Fig. 18 depicts the distribution of the heterogeneity coefficients of different ground objects.

To evaluate the estimate results of the aforementioned methods, the Yamaguchi four-component decomposition with rotation [26] was adopted in the remaining sections. Zoom-in views of three subregions of the decomposition results are illustrated in Fig. 19. It is clear that SCM resulted in the greatest smoothness yet lost much structural details. For example, the housing areas [see Fig. 19(a)] are diffused, and the point target [see Fig. 19(e)] is blurred. In contrast, FP retained most of the fine details, including noise, as shown in Fig. 19(b), (f), and (j). The Lee sigma filtering and our ACoME methods were able to handle both homogeneous and heterogeneous objects with success. However, the Lee sigma filtering exhibited inconsistency

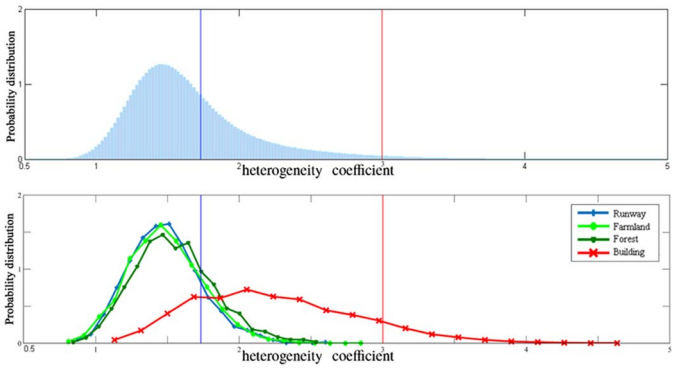

Fig. 18. Heterogeneity coefficient distribution. (Top panel) Distribution of the entire ESAR image. (Bottom panel) Distributions of different land objects. The vertical lines in each plot mark the thresholds, i.e., C^- (blue) and C^+ (red).

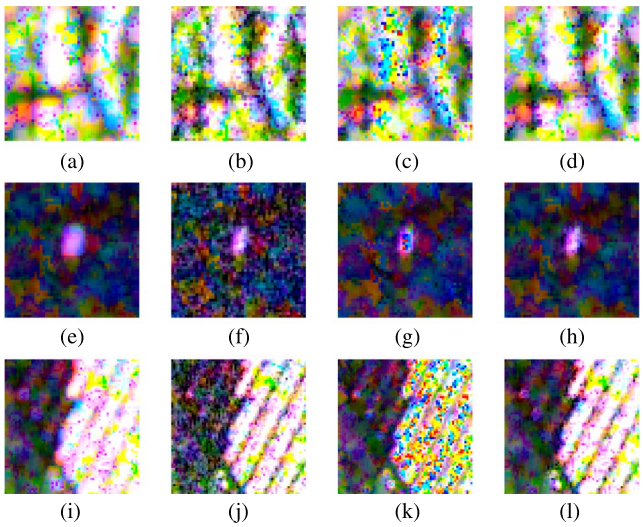

Fig. 19. Zoom-in views of the results of the Yamaguchi decomposition with rotation (red: double component; green: volume component; blue: odd component) using the SCM, FP, Lee sigma filtering, and ACoME methods. The panels depict (a)–(d) housing area, (e)–(h) double-bounce reflector, and (i)–(l) parking lot with rows of cars.

in the results. For example, in Fig. 19(g), the point target is a double-bounce reflector according to Lee and Pottier [8]. The blue pixels in the point target indicate odd component, which is obviously overestimated. In general, ACoME achieved the best performance in preserving both the spatial and polarimetric information.

To quantitatively evaluate the performance of dealing with homogeneous and heterogeneous ground objects, we adopted image ratio and ENL in our experiments. Speckle noise in a polarimetric SAR image follows a multiplication model. Hence, the ratio of the clean image and the processed image characterizes structural preservation. The image ratio r is hence computed as follows [32]:

$$r = \left|1 - \frac{\hat{y}(t)}{y(t)}\right| = \frac{|y(t) - \hat{y}(t)|}{y(t)} \tag{35}$$

where $y(t)$ denotes the origin image, and $\hat{y}(t)$ denotes the processed image. When the structural details are perfectly retained, this ratio yields a zero. A ratio that is deviated from

TABLE VI
INDEXES OF EVALUATION OF ESTIMATIONS. EACH METRIC CONTAINS THREE CASES, AND THE AVERAGE IS CALCULATED FOR COMPARISON

		SCM	FP	Sigma	ACoME
Image ratio	Case 1	0.1373	0.0583	0.0807	0.0785
	Case 2	0.2262	0.0786	0.1074	0.0409
	Case 3	0.2980	0.1307	0.0777	0.0007
	mean	0.2205	0.0892	<u>0.0886</u>	**0.0400**
ENL	Case 4	20.983	2.786	14.535	20.651
	Case 5	16.789	2.587	12.071	16.074
	Case 6	17.903	2.959	11.221	17.846
	mean	**18.558**	2.777	12.609	<u>18.191</u>

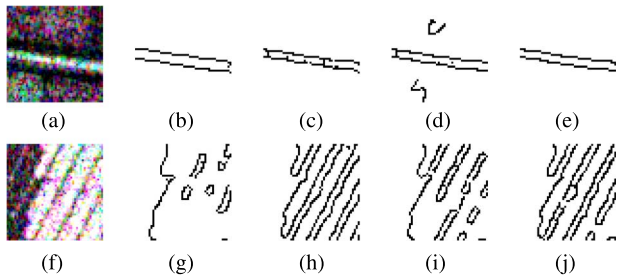

Fig. 20. Zoom-in views of the edge map from the processed images using the SCM, FP, Lee sigma filtering, and ACoME methods. (a) PauliRGB image with homogeneous features. (f) PauliRGB image with heterogeneous features. (b)–(e) and (g)–(j) Edge maps of the processed results using the SCM, FP, Lee sigma filtering, and ACoME methods, respectively.

zero indicates less effectivity in preserving details. This metric is most applicable to the evaluation of the edge preservation of heterogeneous regions. ENL, on the other hand, is an indicator [33] of noise suppression in homogeneous areas, and its computation is given in (24).

Table VI lists our quantitative results. The best and second best results are highlighted in bold and underline, respectively. The image ratio was calculated for cases with heterogeneous areas. In terms of detail preservation, ACoME yielded the best image ratio (0.04) among the four methods. Lee sigma filtering also performed well with a ratio of 0.0886, whereas SCM had the least structural preservation. It is evident that ACoME is superior in handling heterogeneous regions. Table VI also gives the ENL results for cases with homogeneous areas. A greater ENL value indicates better noise suppression in homogeneous regions. SCM attained the greatest ENL, and ACoME attained the second best, with a difference of 1.98% to SCM, which suggests that ACoME is very competitive in handling homogeneous regions.

To compare the performance of retaining details at the boundaries, we adopt a Canny edge detector [34] and illustrate the results in Fig. 20. The threshold used in the Canny edge detector was 0.7 for all cases. The top row gives an input image with mostly homogeneous features and the edge map of the processed images; the bottom row gives the input image with mostly heterogeneous features and the edge map of the processed images. In the homogeneous case, ACoME and SCM retain fine details nearly perfectly [see Fig. 20(a)–(e)], although the averaging effect of SCM widens the target. The FP and Sigma methods were also able to retain boundaries; however, there exists much distortion. In processing the heterogeneous

(a) (b) (c)

Fig. 21. Zoom-in views of the estimate results (PauliRGB) using the ACoME method with different λ. Depicted in (a)–(c) are parking lot with rows of cars. (a) $\lambda = 1$. (b) $\lambda = 3$. (c) $\lambda = 5$.

TABLE VII
QUANTITATIVE EVALUATION OF RESULTS USING DIFFERENT λ VALUES

	$\lambda = 1$	$\lambda = 3$	$\lambda = 5$
Image ratio	0.100	**0.035**	0.112
ENL	9.592	14.449	**14.575**

case, FP and ACoME both achieved much better performance in retaining details while suppressing noise. There exist disconnections in the edge map from the result of our AcoME, whereas unwanted distortions exist in the edge map from the result of the FP method.

F. Analysis of λ for ACoME Estimation

In our ACoME method, C^- and C^+ decide the range of the mixture of homogeneous and heterogeneous components. While C^- is determined by the dimension and number of looks, C^+ is regulated by the free parameter λ, as shown in (23). In this experiment, we evaluate the results of ACoME qualitatively and quantitatively with respect to various λ. When λ is set to 1, C^+ matches C^-, and hence, ACoME degenerates to a dichotomize method that treats the ground regions as either homogeneous or heterogeneous. As we increase λ, we make the criterion more stringent for deciding strict heterogeneous regions.

Fig. 21 depicts the results of the ACoME method using different λ. The panels show zoom-in views of rows of cars (in light color) and parking lot (in dark color). As we increased λ from 1 to 5, the suppression of speckles improved. This is clearly demonstrated in the parking lot region of the zoom-in view. The distortions across the region were much reduced when λ was set to 5. However, the fine structures of the rows of cars were also heavily diffused with λ at 5, and as λ increases, the oversmoothing effect intensifies. In contrast, when λ was set to 1, rows of cars and other ground features were well retained. As shown in Fig. 21(b), λ at 3 yielded the most plausible balance of retaining fine structures and speckle removal.

Table VII lists the quantitative evaluation results using image ratio and ENL. The best results with respect to each metric are highlighted in bold. Among the three λ values, $\lambda = 3$ yielded the smallest image ratio, which implies the greatest similarity to the original image. Both $\lambda = 1$ and $\lambda = 5$ resulted in a much higher image ratio. The oversmoothing effect makes $\lambda = 5$ the least favorable choice. According to ENL, λ at 3 and 5 gave much higher results. Both of these two choices are equally good, and $\lambda = 5$ was at a slightly greater advantage. The difference between the results using $\lambda = 3$ and $\lambda = 5$ is merely 0.86%. This indicates that, when λ is above 3, ACoME is about equally effective in suppressing speckle noise.

IV. CONCLUSION

High-resolution polarimetric SAR images usually contain a mixture of homogeneous and heterogeneous regions. The complexity makes estimation of the underlying coherency matrix a very challenging task. In this paper, we have proposed heterogeneity coefficient based on local coefficient of variation, which describes the degree of heterogeneity of a local area. Our ACoME method employs local heterogeneity coefficient and leverages the advantages of SCM estimation to the homogeneous components and of fixed-point estimation to the heterogeneous components. The optimal coherency matrix estimation is a weighted summation of the estimations to the mixture of scattering components.

Our proposed heterogeneity coefficient provides a means of characterizing the scattering property of ground objects, which enables adaptive estimation of coherency matrix in high-resolution polarimetric SAR imagery. The heterogeneity thresholds were able to adapt to the scattering property and ENL.

Using synthetic SAR imagery and real-world polarimetric SAR imagery of different sensors, we demonstrated that ACoME achieved the best performance with respect to suppressing speckles, retaining the spatial structure, and preserving polarimetric information for both single- and multilook SAR imagery with different degrees of heterogeneity. We also demonstrated the effectiveness of ACoME when dealing with high-resolution polarimetric imagery. The quantitative evaluation affirmed significant improvement. The influence of λ on ACoME was also evaluated and discussed.

ACKNOWLEDGMENT

The authors would like to thank the anonymous reviewers and the associate editor for the helpful comments and suggestions.

REFERENCES

[1] J. W. Goodman, "Some fundamental properties of speckle," *J. Opt. Soc. Amer.*, vol. 66, no. 11, pp. 1145–1150, Nov. 1976.
[2] V. Akbari, A. P. Doulgeris, G. Moser, T. Eltoft, S. N. Anfinsen, and S. B. Serpico, "A textural-contextual model for unsupervised segmentation of multipolarization synthetic aperture radar images," *IEEE Trans. Geosci. Remote Sens.*, vol. 51, no. 4, pp. 2442–2453, Apr. 2013.
[3] G. Vasile, J. Ovarlez, F. Pascal, and C. Tison, "Coherency matrix estimation of heterogeneous clutter in high-resolution polarimetric SAR images," *IEEE Trans. Geosci. Remote Sens.*, vol. 48, no. 4, pp. 1809–1826, Apr. 2010.
[4] J. S. Lee, M. R. Grunes, and G. D. Grandi, "Polarimetric SAR speckle filtering and its impact on terrain classification," *IEEE Trans. Geosci. Remote Sens.*, vol. 37, no. 5, pp. 2363–2373, Sep. 1999.
[5] J. S. Lee, T. L. Ainsworth, Y. T. Wang, and K. S. Chen, "Polarimetric SAR speckle filtering and the extended sigma filter," *IEEE Trans. Geosci. Remote Sens.*, vol. 53, no. 3, pp. 1150–1160, Mar. 2015.
[6] Z. G. Ding, T. Zeng, F. Dong, L. S. Liu, W. F. Yang, and T. Long, "An improved PolSAR image speckle reduction algorithm based on structural judgment and hybrid four-component polarimetric decomposition," *IEEE Trans. Geosci. Remote Sens.*, vol. 51, no. 8, pp. 4438–4449, Aug. 2013.
[7] G. Vasile, F. Pascal, J. Ovarlez, P. Formont, and M. Gay, "Optimal parameter estimation in heterogeneous clutter for high-resolution polarimetric SAR data," *IEEE Geosci. Remote Sens. Lett.*, vol. 8, no. 6, pp. 1046–1050, Nov. 2011.
[8] J. S. Lee and E. Pottier, *Polarimetric Radar Imaging: From Basics to Applications*. Boca Raton, FL, USA: CRC Press, 2009.

[9] N. R. Goodman, "Statistical analysis based on a certain multivariate complex Gaussian distribution (an introduction)," *Ann. Math. Statist.*, vol. 34, no. 1, pp. 152–177, Mar. 1963.
[10] F. Gini and M. Greco, "Covariance matrix estimation for CFAR detection in correlated heavy tailed clutter," *Signal Process.*, vol. 82, no. 12, pp. 1847–1859, Dec. 2002.
[11] S. W. Chen, X. S. Wang, and M. Sato, "PolInSAR complex coherence estimation based on covariance matrix similarity test," *IEEE Trans. Geosci. Remote Sens.*, vol. 50, no. 11, pp. 4699–4710, Nov. 2012.
[12] M. S. Greco and F. Gini, "Statistical analysis of high-resolution SAR ground clutter data," *IEEE Trans. Geosci. Remote Sens.*, vol. 45, no. 3, pp. 566–575, Mar. 2007.
[13] F. T. Ulaby, F. Kouyate, B. Brisco, and T. H. L. Williams, "Textural information in SAR images," *IEEE Trans. Geosci. Remote Sens.*, vol. GE-24, no. 2, pp. 235–245, Mar. 1986.
[14] K. Yao, "A representation theorem and its applications to spherically-invariant random processes," *IEEE Trans. Inf. Theory*, vol. IT-19, no. 5, pp. 600–608, Sep. 1973.
[15] F. Pascal, Y. Chitour, J. P. Ovarlez, P. Forster, and P. Larzabal, "Covariance structure maximum-likelihood estimates in compound Gaussian noise: Existence and algorithm analysis," *IEEE Trans. Signal Process.*, vol. 56, no. 1, pp. 34–48, Jan. 2008.
[16] L. M. Novak and M. C. Burl, "Optimal speckle reduction in polarimetric SAR imagery," *IEEE Trans. Aerosp. Electron. Syst.*, vol. 26, no. 2, pp. 293–305, Mar. 1990.
[17] A. Lopes, R. Touzi, and E. Nezry, "Adaptive speckle filters and scene heterogeneity," *IEEE Trans. Geosci. Remote Sens.*, vol. 28, no. 6, pp. 992–1000, Nov. 1990.
[18] M. Beauchemin, K. P. B. Thomson, and G. Edwards, "The ratio of the arithmetic to the geometric mean: A first-order statistical test for multilook SAR image homogeneity," *IEEE Trans. Geosci. Remote Sens.*, vol. 34, no. 2, pp. 604–606, Mar. 1996.
[19] A. Lopes and F. Sery, "Optimal speckle reduction for the product model in multilook polarimetric SAR imagery and the Wishart distribution," *IEEE Trans. Geosci. Remote Sens.*, vol. 35, no. 3, pp. 632–647, May 1997.
[20] S. Khan and R. Guida, "On fractional moments of multilook polarimetric whitening filter for polarimetric SAR data," *IEEE Trans. Geosci. Remote Sens.*, vol. 52, no. 6, pp. 3502–3512, Sep. 2014.
[21] R. Touzi, A. Lopes, and P. Bousquet, "A statistical and geometrical edge detector for SAR images," *IEEE Trans. Geosci. Remote Sens.*, vol. 26, no. 6, pp. 764–773, Nov. 1988.
[22] S. N. Anfinsen and T. Eltoft, "Application of the matrix-variate Mellin transform to analysis of polarimetric radar images," *IEEE Trans. Geosci. Remote Sens.*, vol. 49, no. 6, pp. 2281–2295, Jun. 2011.
[23] F. Pascal, P. Forster, J. P. Ovarlez, and P. Larzabal, "Performance analysis of covariance matrix estimates in impulsive noise," *IEEE Trans. Signal Process.*, vol. 56, no. 6, pp. 2206–2217, Jun. 2008.
[24] J. S. Lee, D. L. Schuler, R. H. Lang, and K. J. Ranson, "K-distribution for multi-look processed polarimetric SAR imagery," in *Proc. IEEE Int. Geosci. Remote Sens. Symp.*, Pasadena, CA, USA, 1994, vol. 4, pp. 2179–2181.
[25] Y. Yamaguchi, T. Moriyama, M. Ishido, and H. Yamada, "Four-component scattering model for polarimetric SAR image decomposition," *IEEE Trans. Geosci. Remote Sens.*, vol. 43, no. 8, pp. 1699–1706, Aug. 2005.
[26] Y. Yamaguchi, A. Sato, W. M. Borner, R. Sato, and H. Yamada, "Four-component scattering power decomposition with rotation of coherency matrix," *IEEE Trans. Geosci. Remote Sens.*, vol. 49, no. 6, pp. 2251–2258, Jun. 2011.
[27] J. S. Lee, T. L. Ainsworth, and Y. T. Wang, "Generalized polarimetric model-based decompositions using incoherent scattering models," *IEEE Trans. Geosci. Remote Sens.*, vol. 52, no. 5, pp. 2474–2491, May 2014.
[28] J. J. Van Zyl, M. Arii, and Y. Kim, "Model-based decomposition of polarimetric SAR covariance matrices constrained for nonnegative eigenvalues," *IEEE Trans. Geosci. Remote Sens.*, vol. 49, no. 9, pp. 3452–3459, Sep. 2011.
[29] S. W. Chen, Y. Z. Li, X. S. Wang, S. P. Xiao, and M. Sato, "Modeling and interpretation of scattering mechanisms in polarimetric synthetic aperture radar: Advances and perspectives," *IEEE Signal Process. Mag.*, vol. 31, no. 4, pp. 79–89, Jul. 2014.
[30] S. W. Chen, X. S. Wang, S. P. Xiao, and M. Sato, "General polarimetric model-based decomposition for coherency matrix," *IEEE Trans. Geosci. Remote Sens.*, vol. 52, no. 3, pp. 1843–1855, Mar. 2014.
[31] X. G. Liu, Q. Xu, Q. H. Chen, and Q. Chen, "Segmentation of polarimetric SAR images selectively using Wishart and k statistical description," *J. Univ. Electron. Sci. Technol. China*, to be published.
[32] M. Hebar, D. Gleich, and Z. Cucej, "Autobinomial model for SAR image despeckling and information extraction," *IEEE Trans. Geosci. Remote Sens.*, vol. 47, no. 8, pp. 2818–2835, Aug. 2009.
[33] S. Foucher and C. Lopez-Martinez, "Analysis, evaluation, and comparison of polarimetric SAR speckle filtering techniques," *IEEE Trans. Geosci. Remote Sens.*, vol. 23, no. 4, pp. 1751–1764, Apr. 2014.
[34] J. Canny, "A computational approach to edge detection," *IEEE Trans. Pattern Anal. Mach. Intell.*, vol. PAMI-8, no. 6, pp. 679–698, Nov. 1986.

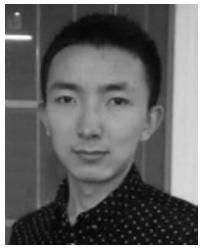

Shuai Yang (S'16) received the B.E. degree in geographical information system from Taiyuan University of Technology, Taiyuan, China, in 2013. He is currently working toward the Ph.D. degree in the Faculty of Information Engineering, China University of Geosciences (CUG), Wuhan, China.

His research interests include polarimetric SAR information extraction, speckle filtering, target decomposition, image segmentation, and the applications of polarimetric SAR.

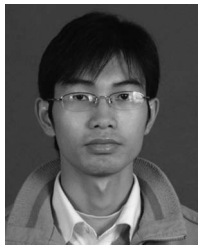

Qihao Chen (M'16) received the B.E. degree in geographic information system and the M.E. and Ph.D. degrees in cartography and geographic information engineering from the China University of Geosciences (CUG), Wuhan, China, in 2004, 2007, and 2011, respectively.

He is currently a Lecturer with the Faculty of Information Engineering, CUG. His research interests include polarimetric synthetic aperture radar, disaster investigation, and assessment.

Xiaohui Yuan (S'01–M'05–SM'16) received the B.S. degree in electrical engineering from Hefei University of Technology, Hefei, China, in 1996 and the Ph.D. degree in computer science from Tulane University, New Orleans, LA, USA, in 2004.

He is currently an Associate Professor with the University of North Texas, Denton, TX, USA, where he is also the Founder and Director of the Computer Vision and Intelligent Systems Laboratory. He is also currently a Visiting Professor with the China University of Geosciences, Wuhan, China. His research interests include computer vision, data mining, machine learning, and artificial intelligence.

Xiuguo Liu (M'16) received the B.E. and M.E. degrees in computer and application and the Ph.D. degree in cartography and geographic information engineering from the China University of Geosciences (CUG), Wuhan, China, in 1991, 1999, and 2004, respectively.

He is currently a Professor and an Associate Dean with the Faculty of Information Engineering, CUG. His research interests include polarimetric synthetic aperture radar theories, geographic information utilization, and 3-D geological modeling.